
Knowing what you know in brain segmentation using Bayesian deep neural networks

Patrick McClure^{1,2}, Nao Rho^{1,2}, John A. Lee^{2,3}, Jakub R. Kaczmarzyk⁴, Charles Zheng^{1,2}, Satrajit S. Ghosh⁴, Dylan M. Nielson^{2,3}, Adam G. Thomas³, Peter Bandettini², Francisco Pereira^{1,2}

¹*Machine Learning Team, National Institute of Mental Health, Bethesda, MD, USA*

²*Section on Functional Imaging Methods, National Institute of Mental Health, Bethesda, MD, USA*

³*Data Sharing and Science Team, National Institute of Mental Health, Bethesda, MD, USA*

⁴*McGovern Institute for Brain Research, Massachusetts Institute of Technology, Cambridge, MA, USA*

Correspondence*:
Patrick McClure
patrick.mcclure@nih.gov

ABSTRACT

In this paper, we describe a deep neural network for predicting FreeSurfer segmentations of structural MRI volumes, in seconds rather than hours. The network was trained and evaluated on an extremely large dataset ($n = 11,148$), obtained by combining data from more than a hundred sites. We also show that the prediction uncertainty of the network at each voxel is a good indicator of whether the network has made an error. The resulting uncertainty volume can be used in conjunction with the predicted segmentation to improve downstream uses. These include the calculation of measures derived from segmentation regions of interest, easing the process of manual annotation by providing both a starting segmentation and an indication of where human attention is required, or the building of prediction models, among many others. We also demonstrate that the average prediction uncertainty across voxels in the brain is an excellent indicator of manual quality control ratings, outperforming a recently published method that combines a wide range of automated QC algorithms. Finally, we show that a Bayesian deep neural network trained using spike-and-slab dropout with learned model uncertainty improves both the segmentation performance and the usefulness of prediction uncertainties. The key results of this paper are general, and should apply to any new network architecture for addressing the segmentation problem.

Keywords: brain segmentation, deep learning, magnetic resonance imaging, bayesian neural networks, variational inference, automated quality control

1 INTRODUCTION

Segmentation of structural magnetic resonance imaging (sMRI) volumes is an essential processing step in neuroimaging analyses. These segmentations are often generated using the FreeSurfer package (Fischl, 2012), a process which can take a day or more for each subject (FreeSurfer, 2018). The computational resources for doing this at a scale of hundreds to thousands of subjects are beyond the capabilities of most sites. This has led to an interest in the use of deep neural networks as a general approach for learning to predict the outcome of a processing task, given the input data, in a much shorter time period than the processing would normally take. In particular, several deep neural networks have been trained to perform segmentation of brain sMRI volumes (Ronneberger et al., 2015; Roy et al., 2018b; Fedorov et al., 2017b,a; Li et al., 2017; Dolz et al., 2018), taking between a few seconds and a few minutes per volume. These networks *directly* predict a manual or an automated segmentation from the structural volumes (Roy et al. (2018b), Fedorov et al. (2017b), Fedorov et al. (2017a), and Dolz et al. (2018) used FreeSurfer, and Petersen et al. (2010) used GIF (Cardoso et al., 2015)). These networks, however, have been trained on a limited number (on the order of hundreds) of examples from a limited number of sites, which can lead to poor cross-site generalization for complex segmentation tasks with a large number of classes (McClure et al., 2018). This includes several of the recent DNNs proposed for fine-grain sMRI segmentation. (Note: We focus on DNNs which predict >30 classes.)

Roy et al. (2018b) performed 33 class segmentation using 581 sMRI volumes from the IXI dataset to train an initial model and then fine-tuned on 28 volumes from the MALC dataset (Marcus et al., 2007). They showed an approximately 9.4% average Dice loss on out-of-site data from the ADNI-29 (Mueller et al., 2005), CANDI (Kennedy et al., 2012), and IBSR (Rohlfing, 2012) datasets. Fedorov et al. (2017a) used 770 sMRI volumes from HCP (Van Essen et al., 2013) to train an initial model and then fine-tuned on 7 volumes from the FBIRN dataset (Keator et al., 2016). Li et al. (2017) performed a 160 class segmentation using 443 sMRI volumes from the ADNI dataset (Petersen et al., 2010) for training. Fedorov et al. (2017a) and Li et al. (2017) did not report test results for sites that were not used during training.

These results show that it is possible to train a neural network to carry out segmentation of a sMRI volume. However, they provide a limited indication of whether such a network would work on data from any new site not encountered in training. While fine-tuning on labelled data from new sites can improve performance, even while using small amounts of data (Fedorov et al., 2017a; Roy et al., 2018b; McClure et al., 2018), a robust neural network segmentation tool should generalize to new sites without any further effort. As part of the process of adding segmentation capabilities to the “Neuronets” tool¹, we trained a network to predict FreeSurfer segmentations given a training set of $\sim 10,000$ sMRI volumes. This paper describes this process, as well as a quantitative and qualitative evaluation of the performance of the resulting model.

Beyond the segmentation performance of the network, a second aspect of interest to us is to understand whether it is feasible for a network to indicate how confident it is about its prediction at each location in the brain. We expect the network to make errors, be it because of noise, unusual positioning of the brain, very different contrast than what it was trained on, etc. Because our model is probabilistic and seeks to learn uncertainties, we expect it to be less confident in its predictions in such cases. While prediction uncertainty can be computed for standard neural networks, as done by Dolz et al. (2018), these uncertainty estimates are often overconfident (Guo et al., 2017; McClure and Kriegeskorte, 2017). Bayesian neural networks (BNNs) have been proposed as a solution to this issue. One popular BNN approach is Monte-Carlo (MC) Bernoulli

¹ <https://github.com/neuronets>

Dropout (Srivastava et al., 2014; Gal and Ghahramani, 2016). Using this method, Li et al. (2017); Roy et al. (2018a) showed that the segmentation performance of the BNN predictions was better for voxels with low dropout sampling-based uncertainties and that injected input noise can lead to increased uncertainty. Roy et al. (2018a) also found that using MC Bernoulli dropout decreased the drop in segmentation performance from 9.4% to 7.8% on average when testing on data from new sites compared to Roy et al. (2018b). However, MC Bernoulli dropout does not learn dropout probabilities from data. Recent works has shown that these dropout probabilities can be learned using a concrete relaxation (Gal et al., 2017). Additionally, learning individual uncertainties for each weight has been shown to be beneficial for many purposes (e.g. pruning and continual learning) (Blundell et al., 2015; Nguyen et al., 2018; McClure et al., 2018). In this paper, we propose using both learned dropout uncertainties and individual weight uncertainties.

Finally, we test the hypothesis that overall prediction uncertainty across an entire image reflects its “quality”, as measured by human quality control (QC) scores. Given the effort required to produce such scores, there have been multiple attempts to either crowdsource the process (Keshavan et al., 2018) or automate it (Esteban et al., 2017). The latter, in particular, does not rely on segmentation information, so we believe it is worthwhile to test whether uncertainty derived from segmentation is more effective.

2 METHODS

2.1 Data

2.1.1 Imaging Datasets

We combined several datasets into a single dataset with 11,148 T1 sMRI volumes. Most of these datasets contained data from multiple scanning sites. The joint dataset comprised 611 volumes from the CMI dataset (Alexander et al., 2017), 3,039 volumes from the CoRR dataset (Zuo et al., 2014), 152 volumes from the GSP dataset (Holmes et al., 2015), 956 volumes from the HCP dataset (Van Essen et al., 2013), 178 volumes from the HBNSI dataset (O’Connor et al., 2017), 10 volumes from the Barrios dataset (Vázquez et al., 2016), 1,136 volumes from the NKI dataset (Nooner et al., 2012), 477 volumes from the SALD (Wei et al., 2018), 1,003 volumes from the SLIM dataset, 992 volumes from the ABIDE dataset Di Martino et al. (2014), 719 volumes from the ADHD200 dataset (Bellec et al., 2017), 183 volumes from the Buckner Lab dataset (Biswal et al., 2010), 45 volumes from the ICBM dataset (Mazziotta et al., 2001), 51 volumes from the Gobbini Lab datasets (di Oleggio Castello et al., 2017), 55 volumes from the Haxby Lab datasets (Haxby et al., 2011; Nastase et al., 2017), and 1,873 volumes from the OpenfMRI dataset (Poldrack et al., 2013). The OpenfMRI data included volumes from (Schonberg et al., 2012; Aron et al., 2006; Tom et al., 2007; Xue et al., 2008; Aron et al., 2007; Foerde et al., 2006; Kelly et al., 2008; Mennes et al., 2010, 2011; Hanson et al., 2004; O’toole et al., 2005; Duncan et al., 2009; Wager et al., 2008; Moran et al., 2012; Uncapher et al., 2011; Gorgolewski et al., 2013; Repovs and Barch, 2012; Walz et al., 2013; Velanova et al., 2008; Padmanabhan et al., 2011; Cera et al., 2014; Verstynen, 2014; Gabitov et al., 2015, 2014; Lepping et al., 2016; Hsu et al., 2016; Koenders et al., 2016; Iannilli et al., 2016; Nilsonne et al., 2016; Van Schuerbeek et al., 2016; Stephan-Otto et al., 2017; Dickstein et al., 2016; Kim et al., 2016; Magnotta et al., 2012; DuPre et al., 2016; Gao et al., 2016; Romaniuk et al., 2016; Chanales et al., 2017; Dalenberg et al., 2017; Roy et al., 2017; FitzGerald et al., 2017; Ballard et al., 2017; Gordon et al., 2017; de Araujo et al., 2013; Nastase et al., 2017, 2018; Vidorreta et al., 2017; Bischoff-Grethe et al., 2007; Maclaren et al., 2014; Vidorreta et al., 2013; Connolly et al., 2012; Power et al., 2017; Tadel et al., 2011; Gramfort et al., 2014, 2013). In-site validation and test sets were created from the combined dataset using a 80-10-10 training-validation-test split.

Layer	Filter	Padding	Dilation (l)	Non-linearity
1	96×3^3	1	1	ReLU
2	96×3^3	1	1	ReLU
3	96×3^3	1	1	ReLU
4	96×3^3	2	2	ReLU
5	96×3^3	4	4	ReLU
6	96×3^3	8	8	ReLU
7	96×3^3	1	1	ReLU
8	50×1^3	0	1	Softmax

Table 1. The MeshNet dilated convolutional neural network architecture used for brain segmentation.

We additionally used 418 sMRI volumes from the NNDSP dataset (Lee et al., 2018) as a held-out dataset to test generalization of the network to an unseen site. In addition to sMRI volumes, each NNDSP sMRI volume was given a QC score from 1 to 4, higher scores corresponding to worse scan quality, by two raters (3 if values differed by more than 1), as described in Blumenthal et al. (2002). If a volume had a QC score greater than 2, it was labeled as a bad quality scan; otherwise, the scan was labeled as a good quality scan.

2.1.2 Data Pre-processing

The sMRI volumes were resampled to 1mm isotropic cubic volumes of 256 voxels per side and the voxel intensities were normalized according to Freesurfer’s `mri_convert` with the `conform` flag. Additionally, input volumes were individually z-scored across voxels.

2.1.3 Segmentation Target

We computed 50-class FreeSurfer (Fischl, 2012) segmentations, as in Fedorov et al. (2017a), for all subjects in each of the datasets described earlier. These were used as the labels for prediction. Although, FreeSurfer segmentations may not be perfectly correct, as compared to manual, expert segmentations, using them allowed us to create a large training dataset, as one could not feasibly label it by hand. FreeSurfer trained networks can also outperform FreeSurfer segmentations when compared to expert segmentations (Roy et al., 2018b). The trained network could be fine-tuned with expert small amounts of labeled data, which would likely improve the results (Roy et al., 2018b; McClure et al., 2018).

2.2 Convolutional Neural Network

2.2.1 Architecture

Several deep neural network architectures have been proposed for brain segmentation, such as U-net (Ronneberger et al., 2015), QuickNAT (Roy et al., 2018b), HighResNet (Li et al., 2017) and MeshNet (Fedorov et al., 2017b,a). We chose MeshNet because of its relatively simple structure, its lower number of learned parameters, and its competitive performance, since the computational cost of Bayesian neural networks scales based on structural complexity and number of parameters.

MeshNet uses dilated convolutional layers (Yu and Koltun, 2015) due to the 3D structural nature of sMRI data. Applying a discrete volumetric dilated convolutional layer to one input channel for one weight filter can be expressed as:

$$(\mathbf{w}_f * l \mathbf{h})_{i,j,k} = \sum_{\tilde{i}=-a}^a \sum_{\tilde{j}=-b}^b \sum_{\tilde{k}=-c}^c w_{f,\tilde{i},\tilde{j},\tilde{k}} h_{i-\tilde{i},j-\tilde{j},k-\tilde{k}} = (\mathbf{w}_f * l \mathbf{h})_{\mathbf{v}} = \sum_{\mathbf{t} \in \mathcal{W}_{abc}} w_{f,\mathbf{t}} h_{\mathbf{v}-\mathbf{t}}. \quad (1)$$

where h is the input to the layer, a , b , and c are the bounds for the i , j , and k axes of the filter with weights \mathbf{w}_f , (i, j, k) is the voxel, \mathbf{v} , where the convolution is computed. The set of indices for the elements of \mathbf{w}_f can be defined as $\mathcal{W}_{abc} = \{-a, \dots, a\} \times \{-b, \dots, b\} \times \{-c, \dots, c\}$. The dilation factor, number of filters, and other details of the MeshNet-like architecture that we used for all experiments is shown in Table 1. Note that we increased the number of filters per layer from 72 to 96, compared to Fedorov et al. (2017a) and McClure et al. (2018), since we greatly increased the number of training volumes.

We split each sMRI volume into 512 non-overlapping $32 \times 32 \times 32$ sub-volumes, similarly to (Fedorov et al., 2017b,a), to be used as inputs for the neural network. The prediction target is the corresponding segmentation sub-volume. After generating segmentations for all 512 sub-volumes, these are then assembled into a segmentation of the entire sMRI volume.

$$p(\mathbf{y}_{test}|\mathbf{x}_{test}) \approx p(\mathbf{y}_{test}|\mathbf{x}_{test}, \mathbf{w}^*) \quad (2)$$

2.2.2 Maximum a Posteriori Estimation

When training a neural network, the weights of the network, \mathbf{w} , are often learned using maximum likelihood estimation (MLE). For MLE, $\log p(\mathcal{D}|\mathbf{w})$ is maximized where $\mathcal{D} = \{(\mathbf{x}_1, \mathbf{y}_1), \dots, (\mathbf{x}_N, \mathbf{y}_N)\}$ is the training dataset and $(\mathbf{x}_n, \mathbf{y}_n)$ is the n th input-output example. This often overfits, however, so we used a prior on the network weights, $p(\mathbf{w})$, to obtain a maximum a posteriori (MAP) estimate, by optimizing $\log p(\mathbf{w}|\mathcal{D})$:

$$\mathbf{w}^* = \underset{\mathbf{w}}{\operatorname{argmax}} \sum_{n=1}^N \log p(\mathbf{y}_n|\mathbf{x}_n, \mathbf{w}) + \log p(\mathbf{w}). \quad (3)$$

We used a fully factorized Gaussian prior (i.e. $p(w_{f,\tilde{i},\tilde{j},\tilde{k}}) = \mathcal{N}(0, 1)$). This results in the MAP weights being learned by minimizing the softmax cross-entropy with L2 regularization. At test time, this point estimate approximation, \mathbf{w}^* , is used to make a prediction for new examples:

2.2.3 Approximate Bayesian Inference

In Bayesian inference for neural networks, a distribution of possible weights is learned instead of just a MAP point estimate. Using Bayes' rule, $p(\mathbf{w}|\mathcal{D}) = p(\mathcal{D}|\mathbf{w})p(\mathbf{w})/p(\mathcal{D})$, where $p(\mathbf{w})$ is the prior over weights. However, directly computing the posterior, $p(\mathbf{w}|\mathcal{D})$, is often intractable, particularly for DNNs. As a result, an approximate inference method must be used.

One of the most popular approximate inference methods for neural networks is variational inference, since it scales well to large DNNs. In variational inference, the posterior distribution $p(\mathbf{w}|\mathcal{D})$ is approximated by a learned variational distribution of weights $q_\theta(\mathbf{w})$, with learnable parameters θ . This approximation is enforced by minimizing the Kullback-Leibler divergence (KL) between $q_\theta(\mathbf{w})$, and the true posterior, $p(\mathbf{w}|\mathcal{D})$, $\text{KL}[q_\theta(\mathbf{w})||p(\mathbf{w}|\mathcal{D})]$, which measures how $q_\theta(\mathbf{w})$ differs from $p(\mathbf{w}|\mathcal{D})$ using relative entropy. This is equivalent to maximizing the variational lower bound (Hinton and Van Camp, 1993; Graves, 2011; Blundell et al., 2015; Kingma et al., 2015; Gal and Ghahramani, 2016; Molchanov et al., 2017; Louizos and Welling, 2017), also known as the evidence lower bound (ELBO),

$$\mathcal{L}_{ELBO}(\theta) = \mathcal{L}_{\mathcal{D}}(\theta) - \mathcal{L}_{KL}(\theta), \quad (4)$$

where $\mathcal{L}_{\mathcal{D}}(\theta)$ is

$$\mathcal{L}_{\mathcal{D}}(\theta) = \sum_{n=1}^N \mathbb{E}_{q_{\theta}(\mathbf{w})} [\log p(\mathbf{y}_n | \mathbf{x}_n, \mathbf{w})] \tag{5}$$

and $\mathcal{L}_{KL}(\theta)$ is the KL divergence between the variational distribution of weights and the prior,

$$\mathcal{L}_{KL}(\theta) = \text{KL}[q_{\theta}(\mathbf{w}) || p(\mathbf{w})] \tag{6}$$

, which measures how $q_{\theta}(\mathbf{w})$ differs from $p(\mathbf{w})$ using relative entropy.

Maximizing $L_{\mathcal{D}}$ seeks to learn a $q_{\theta}(\mathbf{w})$ that explains the training data, while minimizing L_{KL} (i.e. keeping $q_{\theta}(\mathbf{w})$ close to $p(\mathbf{w})$) prevents learning a $q_{\theta}(\mathbf{w})$ that overfits to the training data.

The objective function in Eq. 4 is usually impractical to compute for deep neural networks, due to both: (1) being a full-batch approach and (2) integrating over $q_{\theta}(\mathbf{w})$. (1) is often dealt with by using stochastic mini-batch optimization (Robbins and Monro, 1951) and (2) is often approximated using Monte Carlo sampling. As discussed in Graves (2011); Kingma et al. (2015), these methods can be used to perform stochastic gradient variational Bayes (SGVB) in deep neural networks. For each parameter update, an unbiased estimate of $\nabla_{\theta} \mathcal{L}_{\mathcal{D}}$ for a mini-batch, $\{(\mathbf{x}_1, \mathbf{y}_1), \dots, (\mathbf{x}_M, \mathbf{y}_M)\}$, is calculated using one weight sample, \mathbf{w}_m , from $q_{\theta}(\mathbf{w})$ for each mini-batch example. This results in the following approximation to Eq. 4:

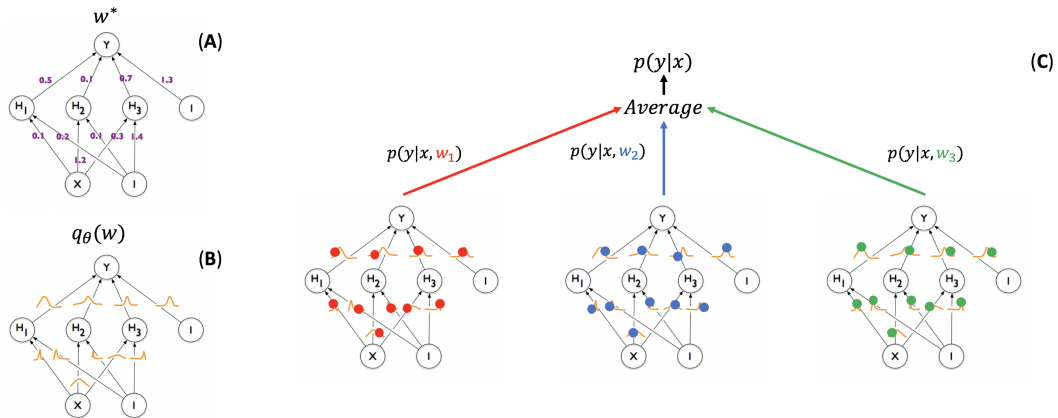


Figure 1. Illustration of generating a prediction from a Bayesian neural network using Monte Carlo sampling (modified from Blundell et al. (2015)). A standard neural network (A, top left) has one weight for each of its connections (w^*), learned from the training set and used in generating a prediction for a test example. A Bayesian neural network (B, bottom left) has, instead, a posterior distribution for each weight, parameterized by theta ($q_{\theta}(w)$). The process of training starts with an assigned prior distribution for each weight, and returns an approximate posterior distribution. At test time (C, right), a weight sample w_1 (red) is drawn from the posterior distribution of the weights, and the resulting network is used to generate a prediction $P(y|x, w_1)$ for an example x . The same can be done for samples w_2 (blue) and w_3 (green), yielding predictions $P(y|x, w_2)$ and $P(y|x, w_3)$, respectively. The three networks are treated as an ensemble and their predictions averaged.

$$\mathcal{L}_{ELBO}(\theta) \approx \mathcal{L}_{\mathcal{D}}^{SGVB}(\theta) - \mathcal{L}_{KL}(\theta), \quad (7)$$

where

$$\mathcal{L}_{\mathcal{D}}(\theta) \approx \mathcal{L}_{\mathcal{D}}^{SGVB}(\theta) = \frac{N}{M} \sum_{m=1}^M \log p(\mathbf{y}_m | \mathbf{x}_m, \mathbf{w}_m). \quad (8)$$

At test time, the weights, \mathbf{w} would ideally be marginalized out, $p(\mathbf{y}_{test} | \mathbf{x}_{test}) = \int p(\mathbf{y}_{test} | \mathbf{x}_{test}, \mathbf{w}) q_{\theta}(\mathbf{w}) d\mathbf{w}$, when making a prediction for a new example. However, this is often impractical to compute for DNNs, so a Monte-Carlo approximation is often used. This results in the prediction of a new example being made by averaging the predictions of multiple weight samples from $q_{\theta}(\mathbf{w})$ (Figure 1):

$$p(\mathbf{y}_{test} | \mathbf{x}_{test}) \approx \frac{1}{N_{MC}} \sum_n^{N_{MC}} p(\mathbf{y}_{test} | \mathbf{x}_{test}, \mathbf{w}_n) \quad (9)$$

where $\mathbf{w}_n \sim q_{\theta}(\mathbf{w})$.

2.2.3.1 MC Bernoulli Dropout

For MC Bernoulli dropout (BD) (Gal and Ghahramani, 2016), we drew weights from $q_{\theta}(\mathbf{w})$ by drawing a Bernoulli random variable ($b_{i,j,k} \sim \text{Bern}(p_l)$), where i, j, k are the indices of the volume axes, for every element of the layer, l , input, \mathbf{h} , and then elementwise multiplying \mathbf{b} and \mathbf{h} before applying the next dilated convolutional layer. This effectively sets the filter weights to zero when applied to a dropped element. Gal and Ghahramani (2016) approximated the KLD between this Bernoulli variational distribution and a zero-mean Gaussian by replacing the variational distribution with a mixture of Gaussians, resulting in an L2-like penalty. However, this can lead to pathological behaviour due to Bernoulli distributions not having support over all real numbers (Hron et al., 2018). In Bernoulli dropout, p_l codes for the uncertainty of the weights and is often set layerwise via hyperparameter search. (For our experiments, we found the best value of p to be 0.9 after searching over the values of 0.95, 0.9, 0.75, and 0.5 using the validation set.) However, Bayesian models would ideally learn how uncertain to be for each weight.

2.2.3.2 Spike-and-Slab Dropout with Learned Model Uncertainty

We propose a form of dropout that both learns the dropout probability for each filter using a concrete relaxation of dropout (Gal et al., 2017), and an individual uncertainty for each weight using fully factorized Gaussian (FFG) filters (Graves, 2011; Blundell et al., 2015; Molchanov et al., 2017; Nguyen et al., 2018; McClure et al., 2018). This is in contrast to previous spike-and-slab dropout methods, which did not learn the model (or epistemic) uncertainty (Der Kiureghian and Ditlevsen, 2009; Kendall and Gal, 2017) from data either by learning the dropout probabilities or by learning the variance parameter of the Gaussian components of the weights (McClure and Kriegeskorte, 2017). In our proposed method, we assume each of the F filters are independent (i.e. $p(\mathbf{w}) = \prod_{f=1}^F p(\mathbf{w}_f)$), as done in previous FFG methods (Graves, 2011; Blundell et al., 2015; Molchanov et al., 2017; Nguyen et al., 2018; McClure et al., 2018). We then decompose each filter into a dropout-based component, b_f , and a Gaussian component, \mathbf{g}_f , such that $\mathbf{w}_f = b_f \mathbf{g}_f$. Per this decomposition, we perform variational inference on the joint distribution

of $\{b_1, \dots, b_F, \mathbf{g}_1, \dots, \mathbf{g}_F\}$, instead of on $p(\mathbf{w})$ directly (Titsias and Lázaro-Gredilla, 2011; McClure and Kriegeskorte, 2017). We then assume each element of \mathbf{g}_f is independent (i.e. $p(\mathbf{g}_f) = \prod_{\mathbf{t} \in \mathcal{W}_{abc}} p(g_{f,\mathbf{t}})$), and that each weight is Gaussian (i.e. $g_{f,\mathbf{t}} \sim \mathcal{N}(\mu_{f,\mathbf{t}}, \sigma_{f,\mathbf{t}}^2)$) with learned parameters $\mu_{f,\mathbf{t}}$ and $\sigma_{f,\mathbf{t}}$. Instead of drawing each b_f from $Bern(p_l)$, we draw them from a concrete distribution (Gal et al., 2017) with a learned dropout probability, p_f , for each filter:

$$b_f = \text{sigmoid}\left(\frac{1}{t}(\log p_f - \log(1 - p_f) + \log u - \log(1 - u))\right) \quad (10)$$

where $u \sim \text{Unif}(0, 1)$. This concrete distribution converges to the Bernoulli distribution as the sigmoid scaling parameter, t , goes to zero. (In this paper, we used $t = 0.02$.) As discussed in Kingma et al. (2015) and Molchanov et al. (2017), randomly sampling each $g_{f,\mathbf{t}}$ for each mini-batch example can be computationally expensive, so we used the fact that the sum of independent Gaussian variables is also Gaussian to move the noise from the weights to the convolution operation, as in McClure et al. (2018). For, dilated convolutions and the proposed spike-and-slab variational distribution, this is described by:

$$(\mathbf{w}_f * \mathbf{h})_{\mathbf{v}} = b_f(\mathbf{g}_f * \mathbf{h})_{\mathbf{v}} \quad (11)$$

where

$$(\mathbf{g}_f * \mathbf{h})_{\mathbf{v}} \sim \mathcal{N}(\mu_{f,\mathbf{v}}^*, (\sigma_{f,\mathbf{v}}^*)^2), \quad (12)$$

$$\mu_{f,\mathbf{v}}^* = \sum_{\mathbf{t} \in \mathcal{W}_{abc}} \mu_{f,\mathbf{t}} h_{\mathbf{v}-\mathbf{t}}, \quad (13)$$

and

$$(\sigma_{f,\mathbf{v}}^*)^2 = \sum_{\mathbf{t} \in \mathcal{W}_{abc}} \sigma_{f,\mathbf{t}}^2 h_{\mathbf{v}-\mathbf{t}}^2. \quad (14)$$

For this spike-and-slab dropout (SSD) implementation, we used a spike-and-slab prior, instead of the Gaussian prior used by Gal and Ghahramani (2016) and Gal et al. (2017). Using a spike-and-slab prior with MC Bernoulli dropout was discussed in Gal (2016), but not implemented. As in the variational distribution, each filter is independent in the prior. Per the spike-and-slab decomposition discussed above, the KL-divergence term of the ELBO can be written as

$$\mathcal{L}_{KL}(\theta) = \sum_{f=1}^F \text{KL}[q_{p_f}(b_f)q_{\mu,\sigma}(\mathbf{g}_f) || p(b_f)p(\mathbf{g}_f)], \quad (15)$$

where $\theta = \bigcup_f^F \bigcup_{\mathbf{t} \in \mathcal{W}_{abc}} \{p_f, \mu_{f,\mathbf{t}}, \sigma_{f,\mathbf{t}}\}$ are the learned parameters and $p(b_f)$ and $p(\mathbf{g}_f)$ are priors. Assuming that each weight in a filter is independent, as commonly done in the literature (Graves, 2011; Blundell et al., 2015; Nguyen et al., 2018), allows the term to be rewritten as

$$\mathcal{L}_{KL}(\theta) = \sum_{f=1}^F (\text{KL}[q_{p_f} || p(b_f)] + \sum_{t \in \mathcal{W}_{abc}} \text{KL}[q_{\mu, \sigma}(g_{f,t}) || p(g_{f,t})]). \quad (16)$$

For $\text{KL}[q_{p_f} || p(b_f)]$, we used the KL-divergence between two Bernoulli distributions,

$$\text{KL}[q_{p_f}(b_f) || p(b_f)] = p_f \log \frac{p_f}{p_{prior}} + (1 - p_f) \log \frac{1 - p_f}{1 - p_{prior}}, \quad (17)$$

since we used a relatively small sigmoid scaling parameter. Using $p(g_{f,t}) = \mathcal{N}(\mu_{prior}, \sigma_{prior}^2)$,

$$\text{KL}[q_{\mu, \sigma}(g_{f,t}) || p(g_{f,t})] = \log \frac{\sigma_{prior}}{\sigma_{f,t}} + \frac{\sigma_{f,t}^2 + (\mu_{f,t} - \mu_{prior})^2}{2\sigma_{prior}^2} - \frac{1}{2}. \quad (18)$$

For this paper, the spike-and-slab prior parameters were set as $p_{prior} = 0.5$, $\mu_{prior} = 0$, and $\sigma_{prior} = 0.1$. $p_{prior} = 0.5$ corresponds to a maximum entropy prior (i.e. in the absence of new data be maximally uncertain). Alternatively, a p_{prior} close to 0 is a sparsity prior (i.e. in the absence of data do not use a filter).

2.3 Quantifying performance

2.3.1 Segmentation performance measure

To measure the quality of the produced segmentations, we calculated the Dice coefficient, which is defined by

$$Dice_c = \frac{2|\hat{\mathbf{y}}_c \cdot \mathbf{y}_c|}{\|\hat{\mathbf{y}}_c\|^2 + \|\mathbf{y}_c\|^2} = \frac{2TP_c}{2TP_c + FN_c + FP_c}, \quad (19)$$

where $\hat{\mathbf{y}}_c$ is the binary segmentation for class c produced by a network, \mathbf{y}_c is the ground truth produced by FreeSurfer, TP_c is the true positive rate for class c , FN_c is the false negative rate for class c , and FP_c is the false positive rate for class c . We calculate the Dice coefficient separately for each class $c = 1, \dots, 50$, and average across classes to compute the overall performance of a network for one sMRI volume.

2.3.2 Uncertainty measure

We quantify the uncertainty of a prediction, $p(\mathbf{y}_{m,c} | x_m)$, using the aleatoric uncertainty (Der Kiureghian and Ditlevsen, 2009; Kendall and Gal, 2017), which was measured by the entropy of the softmax across the 50 output classes,

$$H(\mathbf{y}_{m,c} | x_m) = - \sum_{c=1}^{50} p(\mathbf{y}_{m,c} | x_m) \log p(\mathbf{y}_{m,c} | x_m). \quad (20)$$

We calculate the uncertainty for each output voxel separately, and the uncertainty for one sMRI volume by averaging across all output voxels not classified as background (i.e. given the unknown label).

Method	In-site	Out-of-site
MAP	0.7790 ± 0.0576	0.7333 ± 0.0498
BD	0.7764 ± 0.0506	0.7369 ± 0.0474
SSD	0.8373 ± 0.0471	0.7921 ± 0.0444

Table 2. The average and standard deviation of the class Dices across test volumes for the maximum a posteriori (MAP), MC Bernoulli dropout (BD), and spike-and-slab dropout (SSD) network on the in-site and out-of-site test sets.

3 RESULTS

3.1 Segmentation performance

We trained MAP, MC Bernoulli Dropout (BD), and Spike-and-Slab Dropout (SSD) Meshnet-like CNNs on the 9,298 sMRI volumes in the training set. We then applied our networks to produce segmentations for both the in-site test set and the out-of-site test data. For the BD and SSD networks, 10 MC samples were used for test predictions. The means and standard deviations across volumes for the average Dice across all 50 classes are shown in Table 2. Dice scores for each label for the in-site and out-of-site test sets are shown in Figure 2 and 3, respectively. We found that, compared to MAP and BD, SSD significantly increased the Dice for both the in-site ($p < 1e - 6$) and out-of-site ($p < 1e - 6$) test sets, per a paired t-test across test volumes. We found that SSD had a 5.7% drop in performance from the in-site test set to the out-of-site test set, where as the MAP has a drop of 6.2% and BD a drop of 5.4%. This is better than drops of 9.4% and 7.8% on average reported in the literature by Roy et al. (2018b) and Roy et al. (2018a), respectively. In Figures 4 and 5, we show selected example segmentations for the SSD network for volumes that have Dice scores similar to the average Dice score across the respective dataset.

3.2 Utilizing Uncertainty

3.2.1 Predicting segmentation errors from uncertainty

Ideally, an increase in DNN prediction uncertainty indicates an increase in the likelihood that that prediction is incorrect. To evaluate whether this is the case for the trained brain segmentation DNN, we performed a receiver operating characteristic (ROC) analysis. In this analysis, voxels are ranked from most uncertain to least uncertain and one considers, at each rank, what fraction of the voxels were also misclassified by the network. An ROC curve can then be generated by plotting the true positive rate vs the false negative rate for different uncertainty thresholds used to predict misclassification. The area under this curve (AUC) is typically summarized the results of the ROC analysis. The average ROC and AUCs across volumes for MAP, BD, and SSD for the in-site and out-of-site test sets are shown in 6. Compared to MAP and BD, SSD significantly improved the AUC for both the in-site ($p < 1e - 6$) and out-of-site ($p < 1e - 6$) test sets, per a paired t-test across test set volumes.

3.2.2 Predicting scan quality from uncertainty

Ideally, the output uncertainty for inputs not drawn from the training distribution should be relatively high. This could potentially be useful for a variety of applications. One particular application is detection of bad quality sMRI scans, since the segmentation DNN was trained using relatively good quality scans. To test the validity of predicting high vs low quality scans, we performed an ROC analysis on the held-out NNDSP dataset, where manual quality control ratings are available. We also did the same analysis using MRIQC (v0.10.5) Esteban et al. (2017), a recently published method that combines a wide range of automated QC algorithms. To statistically test whether any method significantly outperformed the other methods,

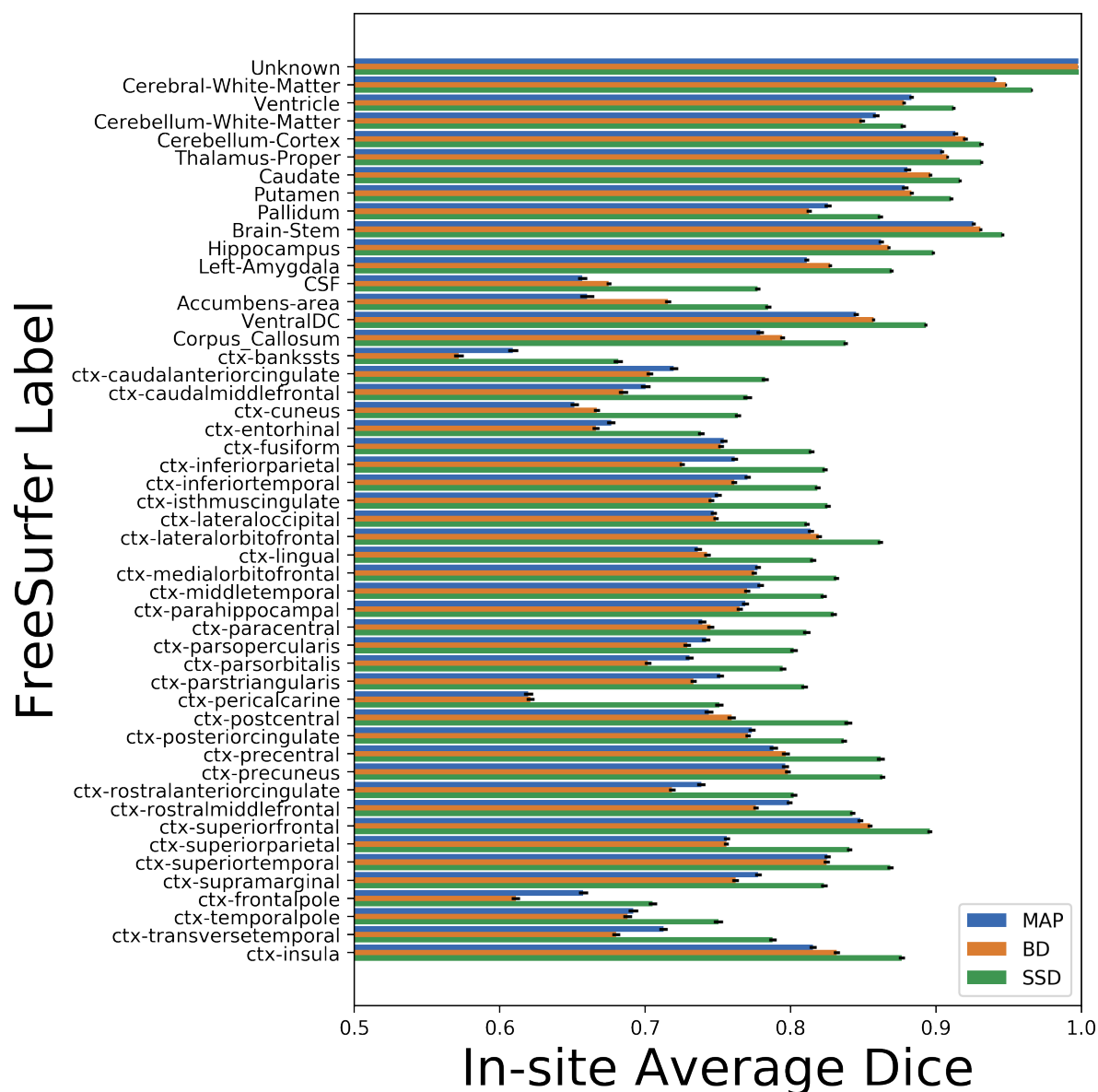


Figure 2. Average Dice scores and standard errors across in-site test volumes for each label for the maximum a posteriori (MAP), MC Bernoulli dropout (BD), and spike-and-slab dropout (SSD) networks.

we performed bootstrap sampling of the AUC for predicting scan quality from average uncertainty by sampling out-of-site test volumes. We performed 10,000 bootstrap samples, each with 418 volumes. The average ROC and AUC for the MAP, BD, SSD, and MRIQC methods are shown in Figure 7. The MAP, BD, and SSD networks all have significantly higher AUCs than MRIQC ($p = 1.369e - 4$, $p = 1.272e - 5$, and $p = 1.381e - 6$, respectively). Additionally, SSD had a significantly higher AUC than both MAP and BD ($p = 1.156e - 3$ and $p = 1.042e - 3$, respectively).

4 DISCUSSION

We trained a standard MAP deep neural network (DNN) to predict FreeSurfer segmentations from structural MRI (sMRI) volumes. We trained on a little under 10,000 sMRIs, obtained by combining 70 different datasets (many of which, in turn, contain images from several sites, scanners, and sequences, e.g. NKI,

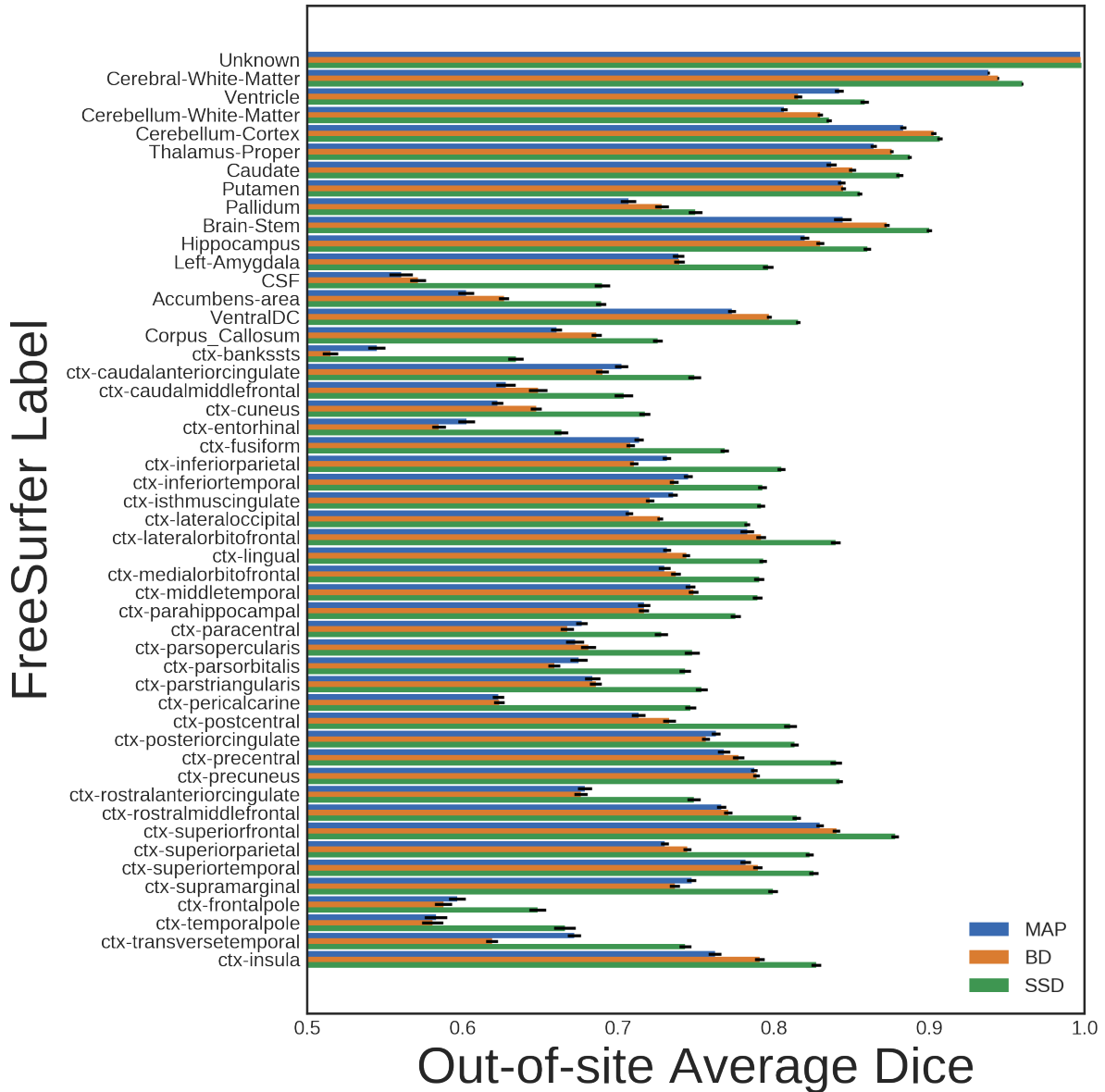


Figure 3. Average Dice scores and standard errors across out-of-site test volumes for each label for the maximum a posteriori (MAP), MC Bernoulli dropout (BD), and spike-and-slab dropout (SSD) networks.

ABIDE, ADHD200). We used a separate test set of more than 1,000 sMRIs, drawn from the same datasets. The resulting standard DNN performs at the same level of state-of-the-art networks (Fedorov et al., 2017a). This result, however, was obtained by testing over two orders of magnitude more test data, and many more sites, than those papers. We also tested performance on a completely separate dataset (NNDSP) from a site not encountered in training, which contained 418 sMRI volumes. Whereas Dice performance dropped slightly, this was less than what was observed in other studies (Roy et al., 2018b,a); this suggests that we may be achieving better generalization by training on our larger and more diverse dataset, and we plan on testing this on more datasets from novel sites in the future. This is particularly important to us, as this network is meant to be used within an off-the-shelf tool².

² :<https://github.com/neuronets/>

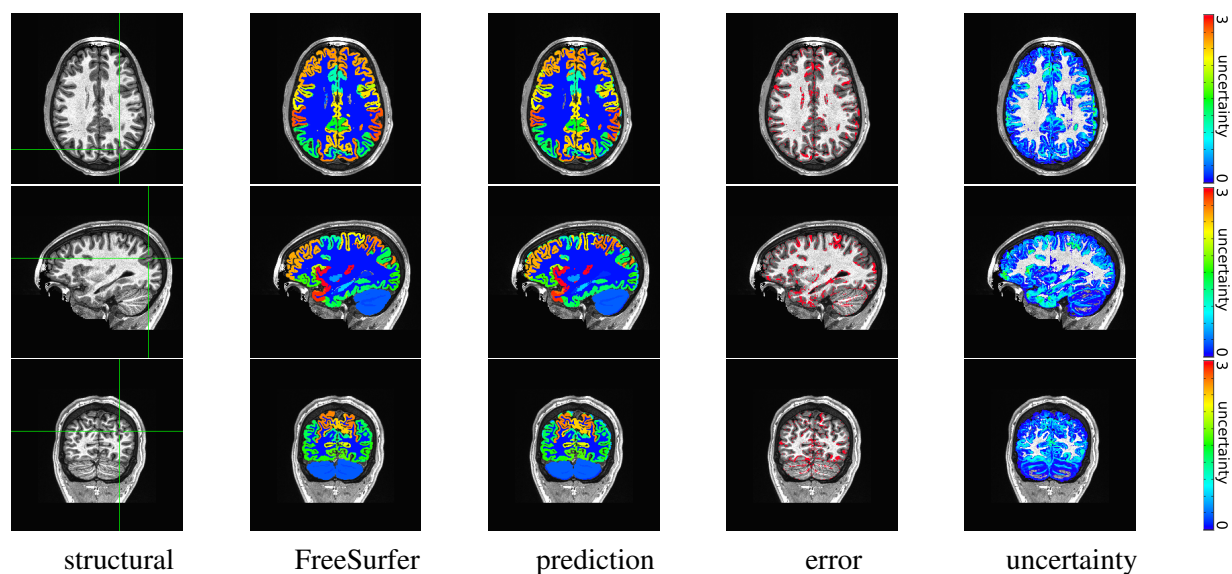


Figure 4. In-site segmentation results for the spike-and-slab dropout (SSD) network for a test subject with average Dice performance. The columns show, respectively, the structural image used as input, the FreeSurfer segmentation used as a prediction target, the prediction made by our network, the voxels where there was a mismatch between prediction and target, and the prediction uncertainty at each voxel.

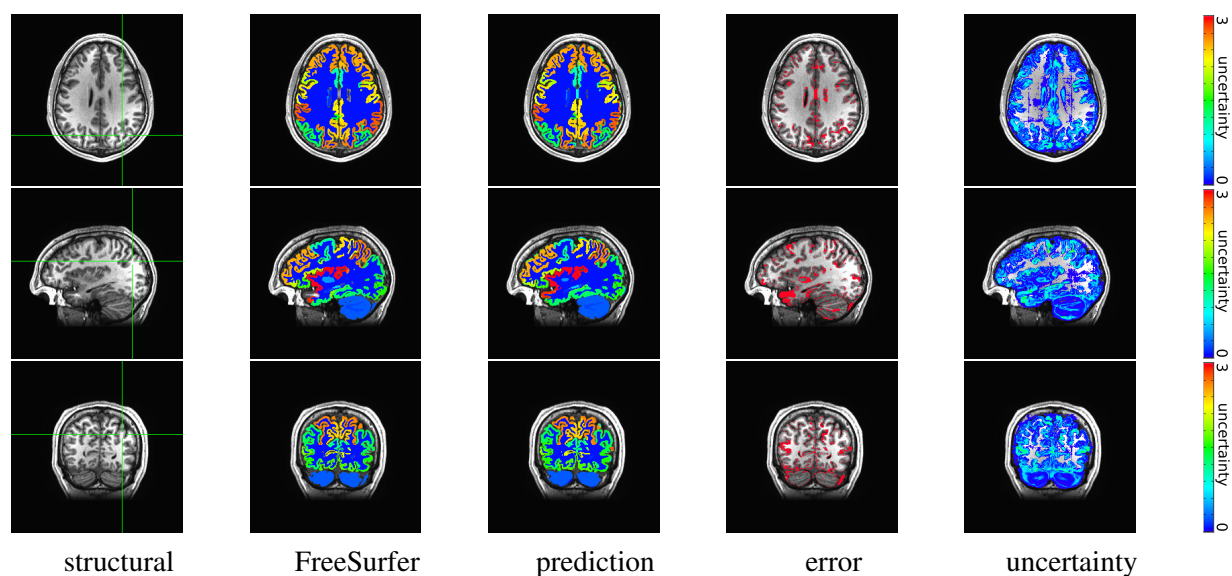


Figure 5. Out-of-site segmentation results for the spike-and-slab dropout (SSD) network for a test subject with average Dice performance. The columns show, respectively, the structural image used as input, the FreeSurfer segmentation used as a prediction target, the prediction made by our network, the voxels where there was a mismatch between prediction and target, and the prediction uncertainty at each voxel.

We believe it may be possible to improve this segmentation processing, in that we did not use registration. One option would be to use various techniques for data augmentation (e.g. variation of image contrast, since that is pretty heterogeneous, rotations/translations of existing examples, addition of realistic noise, etc). Another would be to eliminate the need to divide the brain into sub-volumes, which loses some global information; this will become more feasible in GPUs with more memory. Finally, we plan on using post-processing of results (e.g. ensure some coherence between predictions for adjacent voxels, leverage off-the-shelf brain and tissue masking code).

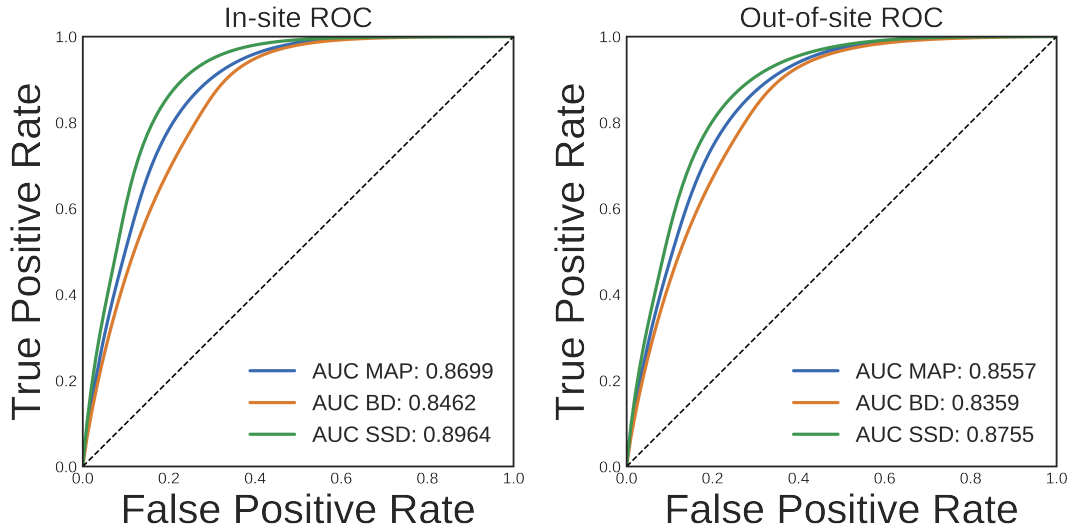


Figure 6. Receiver operating characteristic (ROC) curves for predicting errors for the in-site and out-of-site test sets from the voxel uncertainty of the maximum a posteriori (MAP), MC Bernoulli dropout (BD), and spike-and-slab dropout (SSD) networks.

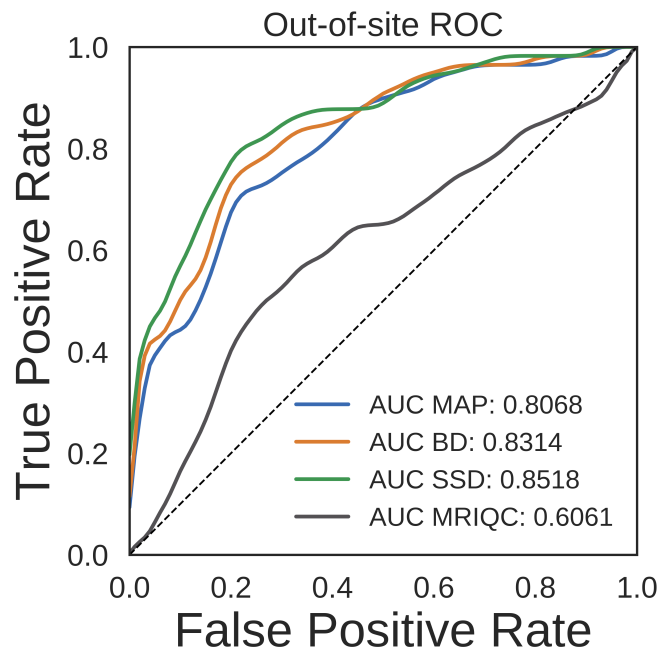


Figure 7. Receiver operating characteristic (ROC) curves for predicting scan quality for the NNDSP out-of-site test set from the average non-background voxel uncertainty of the maximum a posteriori (MAP), MC Bernoulli dropout (BD), and spike-and-slab dropout (SSD) networks and from MRIQC scores.

We demonstrated that the estimated uncertainty for the prediction at each voxel is a good indicator of whether the standard network makes an error in it, both in-site and out-of-site. The tool that produces the predicted segmentation volume for an input sMRI will also produce an uncertainty volume. We anticipate this being useful at various levels, e.g. to refine other tools that rely on segmentation images, or to improve prediction models based on sMRI data (e.g. modification of calculation of cortical thickness, surface area, voxel selection or weighting in regression (Roy et al., 2018a) or classification models, etc).

We also demonstrated that the average prediction uncertainty across voxels in the brain is an excellent indicator of manual quality control ratings. Furthermore, it outperforms the best existing automated solution (Esteban et al., 2017). Since automation is already used in large repositories (e.g. OpenMRI), we plan on offering our tool as an additional quality control measure.

Finally, we developed a new Bayesian DNN using spike-and-slab dropout with learned model uncertainty. This increased segmentation performance and improved the usefulness of output uncertainties compared both to a MAP DNN method and an MC Bernoulli dropout method, which has previously been used in the brain segmentation literature (Li et al., 2017; Roy et al., 2018a). These results show that Bayesian DNNs are a promising method for building brain segmentation and automated sMRI quality control tools.

ACKNOWLEDGMENTS

This research was supported (in part) by the Intramural Research Program of the NIMH (ZICMH002968). This work utilized the computational resources of the NIH HPC Biowulf cluster. (<http://hpc.nih.gov>). JK's and SG's contribution was supported by NIH R01 EB020740.

REFERENCES

- Alexander, L. M., Escalera, J., Ai, L., Andreotti, C., Febre, K., Mangone, A., et al. (2017). An open resource for transdiagnostic research in pediatric mental health and learning disorders. *Scientific data* 4, 170181
- Aron, A. R., Behrens, T. E., Smith, S., Frank, M. J., and Poldrack, R. A. (2007). Triangulating a cognitive control network using diffusion-weighted magnetic resonance imaging (mri) and functional mri. *Journal of Neuroscience* 27, 3743–3752
- Aron, A. R., Gluck, M. A., and Poldrack, R. A. (2006). Long-term test–retest reliability of functional mri in a classification learning task. *Neuroimage* 29, 1000–1006
- Ballard, I. C., Kim, B., Liatsis, A., Aydogan, G., Cohen, J. D., and McClure, S. M. (2017). More is meaningful: the magnitude effect in intertemporal choice depends on self-control. *Psychological science* 28, 1443–1454
- Bellec, P., Chu, C., Chouinard-Decorte, F., Benhajali, Y., Margulies, D. S., and Craddock, R. C. (2017). The neuro bureau adhd-200 preprocessed repository. *Neuroimage* 144, 275–286
- Bischoff-Grethe, A., Ozyurt, I. B., Busa, E., Quinn, B. T., Fennema-Notestine, C., Clark, C. P., et al. (2007). A technique for the deidentification of structural brain mr images. *Human brain mapping* 28, 892–903
- Biswal, B. B., Mennes, M., Zuo, X.-N., Gohel, S., Kelly, C., Smith, S. M., et al. (2010). Toward discovery science of human brain function. *Proceedings of the National Academy of Sciences* 107, 4734–4739
- Blumenthal, J. D., Zijdenbos, A., Molloy, E., and Giedd, J. N. (2002). Motion artifact in magnetic resonance imaging: implications for automated analysis. *Neuroimage* 16, 89–92
- Blundell, C., Cornebise, J., Kavukcuoglu, K., and Wierstra, D. (2015). Weight uncertainty in neural networks. In *International Conference on Machine Learning*. 1613–1622
- Cardoso, M. J., Modat, M., Wolz, R., Melbourne, A., Cash, D., Rueckert, D., et al. (2015). Geodesic information flows: spatially-variant graphs and their application to segmentation and fusion. *IEEE transactions on medical imaging* 34, 1976–1988
- Cera, N., Tartaro, A., and Sensi, S. L. (2014). Modafinil alters intrinsic functional connectivity of the right posterior insula: a pharmacological resting state fmri study. *PLoS One* 9, e107145
- Chanals, A. J., Oza, A., Favila, S. E., and Kuhl, B. A. (2017). Overlap among spatial memories triggers repulsion of hippocampal representations. *Current Biology* 27, 2307–2317

- Connolly, A. C., Guntupalli, J. S., Gors, J., Hanke, M., Halchenko, Y. O., Wu, Y.-C., et al. (2012). The representation of biological classes in the human brain. *Journal of Neuroscience* 32, 2608–2618
- Dalenberg, J. R., Weitkamp, L., Renken, R. J., Nanetti, L., and ter Horst, G. J. (2017). Flavor pleasantness processing in the ventral emotion network. *PloS one* 12, e0170310
- de Araujo, I. E., Lin, T., Veldhuizen, M. G., and Small, D. M. (2013). Metabolic regulation of brain response to food cues. *Current Biology* 23, 878–883
- Der Kiureghian, A. and Ditlevsen, O. (2009). Aleatory or epistemic? does it matter? *Structural Safety* 31, 105–112
- Di Martino, A., Yan, C.-G., Li, Q., Denio, E., Castellanos, F. X., Alaerts, K., et al. (2014). The autism brain imaging data exchange: Towards a large-scale evaluation of the intrinsic brain architecture in autism. *Molecular Psychiatry* 19, 659
- di Oleggio Castello, M. V., Halchenko, Y. O., Guntupalli, J. S., Gors, J. D., and Gobbini, M. I. (2017). The neural representation of personally familiar and unfamiliar faces in the distributed system for face perception. *Scientific Reports* 7
- Dickstein, D., Pullman, M., Fernandez, C., Short, J., Kostakoglu, L., Knesaurek, K., et al. (2016). Cerebral [18 f] t807/av1451 retention pattern in clinically probable cte resembles pathognomonic distribution of cte tauopathy. *Translational psychiatry* 6, e900
- Dolz, J., Desrosiers, C., and Ayed, I. B. (2018). 3d fully convolutional networks for subcortical segmentation in mri: A large-scale study. *NeuroImage* 170, 456–470
- Duncan, K. J., Pattamadilok, C., Knierim, I., and Devlin, J. T. (2009). Consistency and variability in functional localisers. *Neuroimage* 46, 1018–1026
- DuPre, E., Luh, W.-M., and Spreng, R. N. (2016). Multi-echo fmri replication sample of autobiographical memory, prospection and theory of mind reasoning tasks. *Scientific data* 3, 160116
- Esteban, O., Birman, D., Schaer, M., Koyejo, O. O., Poldrack, R. A., and Gorgolewski, K. J. (2017). Mriqc: Advancing the automatic prediction of image quality in mri from unseen sites. *PloS one* 12, e0184661
- Fedorov, A., Damaraju, E., Calhoun, V., and Plis, S. (2017a). Almost instant brain atlas segmentation for large-scale studies. *arXiv preprint arXiv:1711.00457*
- Fedorov, A., Johnson, J., Damaraju, E., Ozerin, A., Calhoun, V., and Plis, S. (2017b). End-to-end learning of brain tissue segmentation from imperfect labeling. In *International Joint Conference on Neural Networks (IEEE)*, 3785–3792
- Fischl, B. (2012). Freesurfer. *Neuroimage* 62
- FitzGerald, T. H., Hämmerer, D., Friston, K. J., Li, S.-C., and Dolan, R. J. (2017). Sequential inference as a mode of cognition and its correlates in fronto-parietal and hippocampal brain regions. *PLoS computational biology* 13, e1005418
- Foerde, K., Knowlton, B. J., and Poldrack, R. A. (2006). Modulation of competing memory systems by distraction. *Proceedings of the National Academy of Sciences* 103, 11778–11783
- FreeSurfer (2018). reconallruntimes Accessed: 2018-12-04
- Gabitov, E., Manor, D., and Karni, A. (2014). Done that: short-term repetition related modulations of motor cortex activity as a stable signature for overnight motor memory consolidation. *Journal of cognitive neuroscience* 26, 2716–2734
- Gabitov, E., Manor, D., and Karni, A. (2015). Patterns of modulation in the activity and connectivity of motor cortex during the repeated generation of movement sequences. *Journal of cognitive neuroscience* 27, 736–751
- Gal, Y. (2016). *Uncertainty in Deep Learning*. Ph.D. thesis, University of Cambridge

- Gal, Y. and Ghahramani, Z. (2016). Dropout as a Bayesian approximation: Representing model uncertainty in deep learning. In *International Conference on Machine Learning*. 1050–1059
- Gal, Y., Hron, J., and Kendall, A. (2017). Concrete dropout. In *Advances in Neural Information Processing Systems*. 3581–3590
- Gao, X., Deng, X., Wen, X., She, Y., Vinke, P. C., and Chen, H. (2016). My body looks like that girl's: Body mass index modulates brain activity during body image self-reflection among young women. *PLoS one* 11, e0164450
- Gordon, E. M., Laumann, T. O., Gilmore, A. W., Newbold, D. J., Greene, D. J., Berg, J. J., et al. (2017). Precision functional mapping of individual human brains. *Neuron* 95, 791–807
- Gorgolewski, K. J., Storkey, A., Bastin, M. E., Whittle, I. R., Wardlaw, J. M., and Pernet, C. R. (2013). A test-retest fmri dataset for motor, language and spatial attention functions. *GigaScience* 2, 6
- Gramfort, A., Luessi, M., Larson, E., Engemann, D. A., Strohmeier, D., Brodbeck, C., et al. (2013). Meg and eeg data analysis with mne-python. *Frontiers in neuroscience* 7, 267
- Gramfort, A., Luessi, M., Larson, E., Engemann, D. A., Strohmeier, D., Brodbeck, C., et al. (2014). Mne software for processing meg and eeg data. *Neuroimage* 86, 446–460
- Graves, A. (2011). Practical variational inference for neural networks. In *Advances in Neural Information Processing Systems*. 2348–2356
- Guo, C., Pleiss, G., Sun, Y., and Weinberger, K. Q. (2017). On calibration of modern neural networks. In *Proceedings of the 34th International Conference on Machine Learning-Volume 70*. 1321–1330
- Hanson, S. J., Matsuka, T., and Haxby, J. V. (2004). Combinatorial codes in ventral temporal lobe for object recognition: Haxby (2001) revisited: is there a “face” area? *Neuroimage* 23, 156–166
- Haxby, J. V., Guntupalli, J. S., Connolly, A. C., Halchenko, Y. O., Conroy, B. R., Gobbini, M. I., et al. (2011). A common, high-dimensional model of the representational space in human ventral temporal cortex. *Neuron* 72, 404–416
- Hinton, G. E. and Van Camp, D. (1993). Keeping the neural networks simple by minimizing the description length of the weights. In *Proceedings of the sixth annual conference on Computational learning theory (ACM)*, 5–13
- Holmes, A. J., Hollinshead, M. O., O’Keefe, T. M., Petrov, V. I., Fariello, G. R., Wald, L. L., et al. (2015). Brain genomics superstruct project initial data release with structural, functional, and behavioral measures. *Scientific data* 2, 150031
- Hron, J., Matthews, A. G., and Ghahramani, Z. (2018). Variational bayesian dropout: pitfalls and fixes. In *International Conference on Machine Learning*. 2024–2033
- Hsu, A.-L., Chou, K.-H., Chao, Y.-P., Fan, H.-Y., Wu, C. W., and Chen, J.-H. (2016). Physiological contribution in spontaneous oscillations: an approximate quality-assurance index for resting-state fmri signals. *PLoS one* 11, e0148393
- Iannilli, E., Gasparotti, R., Hummel, T., Zoni, S., Benedetti, C., Fedrighi, C., et al. (2016). Effects of manganese exposure on olfactory functions in teenagers: a pilot study. *PLoS one* 11, e0144783
- Keator, D. B., van Erp, T. G., Turner, J. A., Glover, G. H., Mueller, B. A., Liu, T. T., et al. (2016). The function biomedical informatics research network data repository. *Neuroimage* 124, 1074–1079
- Kelly, A. C., Uddin, L. Q., Biswal, B. B., Castellanos, F. X., and Milham, M. P. (2008). Competition between functional brain networks mediates behavioral variability. *Neuroimage* 39, 527–537
- Kendall, A. and Gal, Y. (2017). What uncertainties do we need in bayesian deep learning for computer vision? In *Advances in neural information processing systems*. 5574–5584
- [Dataset] Kennedy, D. N., Haselgrove, C., Hodge, S. M., Rane, P. S., Makris, N., and Frazier, J. A. (2012). Candishare: a resource for pediatric neuroimaging data

- Keshavan, A., Yeatman, J., and Rokem, A. (2018). Combining citizen science and deep learning to amplify expertise in neuroimaging. *bioRxiv* doi:10.1101/363382
- Kim, J., Wang, J., Wedell, D. H., and Shinkareva, S. V. (2016). Identifying core affect in individuals from fmri responses to dynamic naturalistic audiovisual stimuli. *PLoS one* 11, e0161589
- Kingma, D. P., Salimans, T., and Welling, M. (2015). Variational dropout and the local reparameterization trick. In *Advances in Neural Information Processing Systems*. 2575–2583
- Koenders, L., Cousijn, J., Vingerhoets, W. A., van den Brink, W., Wiers, R. W., Meijer, C. J., et al. (2016). Grey matter changes associated with heavy cannabis use: a longitudinal smri study. *PLoS One* 11, e0152482
- Lee, J. A., Gustavo, S., Migineishvili, N., Nielson, D., Bandettini, P. A., Shaw, P., et al. (2018). Automated quality control methods applied to a novel dataset. doi:https://doi.org/10.15154/1463004. Organization for Human Brain Mapping (OHBM) Annual Meeting
- Lepping, R. J., Atchley, R. A., Chrysikou, E., Martin, L. E., Clair, A. A., Ingram, R. E., et al. (2016). Neural processing of emotional musical and nonmusical stimuli in depression. *PLoS one* 11, e0156859
- Li, W., Wang, G., Fidon, L., Ourselin, S., Cardoso, M. J., and Vercauteren, T. (2017). On the compactness, efficiency, and representation of 3D convolutional networks: Brain parcellation as a pretext task. In *International Conference on Information Processing in Medical Imaging* (Springer), 348–360
- Louizos, C. and Welling, M. (2017). Multiplicative normalizing flows for variational Bayesian neural networks. In *International Conference on Machine Learning*. 2218–2227
- Maclaren, J., Han, Z., Vos, S. B., Fischbein, N., and Bammer, R. (2014). Reliability of brain volume measurements: A test-retest dataset. *Scientific data* 1, 140037
- Magnotta, V. a., Matsui, J. T., Liu, D., Johnson, H. J., Long, J. D., Bolster, B. D., et al. (2012). Multi-Center Reliability of Diffusion Tensor Imaging. *Brain Connectivity* 2, 121018043201009
- Marcus, D. S., Wang, T. H., Parker, J., Csernansky, J. G., Morris, J. C., and Buckner, R. L. (2007). Open access series of imaging studies (oasis): cross-sectional mri data in young, middle aged, nondemented, and demented older adults. *Journal of cognitive neuroscience* 19, 1498–1507
- Mazziotta, J., Toga, A., Evans, A., Fox, P., Lancaster, J., Zilles, K., et al. (2001). A probabilistic atlas and reference system for the human brain: International consortium for brain mapping (icbm). *Philosophical Transactions of the Royal Society of London B: Biological Sciences* 356, 1293–1322
- McClure, P. and Kriegeskorte, N. (2017). Robustly representing uncertainty in deep neural networks through sampling. In *NIPS Bayesian Deep Learning Workshop*
- McClure, P., Zheng, C. Y., Kaczmarzyk, J., Rogers-Lee, J., Ghosh, S., Nielson, D., et al. (2018). Distributed weight consolidation: A brain segmentation case study. In *Advances in Neural Information Processing Systems 31*, eds. S. Bengio, H. Wallach, H. Larochelle, K. Grauman, N. Cesa-Bianchi, and R. Garnett. 4093–4103
- Mennes, M., Kelly, C., Zuo, X.-N., Di Martino, A., Biswal, B. B., Castellanos, F. X., et al. (2010). Inter-individual differences in resting-state functional connectivity predict task-induced bold activity. *Neuroimage* 50, 1690–1701
- Mennes, M., Zuo, X.-N., Kelly, C., Di Martino, A., Zang, Y.-F., Biswal, B., et al. (2011). Linking inter-individual differences in neural activation and behavior to intrinsic brain dynamics. *Neuroimage* 54, 2950–2959
- Molchanov, D., Ashukha, A., and Vetrov, D. (2017). Variational dropout sparsifies deep neural networks. In *International Conference on Machine Learning*. 2498–2507
- Moran, J. M., Jolly, E., and Mitchell, J. P. (2012). Social-cognitive deficits in normal aging. *Journal of neuroscience* 32, 5553–5561

- Mueller, S. G., Weiner, M. W., Thal, L. J., Petersen, R. C., Jack, C., Jagust, W., et al. (2005). The alzheimer's disease neuroimaging initiative. *Neuroimaging Clinics* 15, 869–877
- Nastase, S. A., Connolly, A. C., Oosterhof, N. N., Halchenko, Y. O., Guntupalli, J. S., Visconti di Oleggio Castello, M., et al. (2017). Attention selectively reshapes the geometry of distributed semantic representation. *Cerebral Cortex* 27, 4277–4291
- Nastase, S. A., Halchenko, Y. O., Connolly, A. C., Gobbini, M. I., and Haxby, J. V. (2018). Neural responses to naturalistic clips of behaving animals in two different task contexts. *Frontiers in neuroscience* 12, 316
- Nguyen, C. V., Li, Y., Bui, T. D., and Turner, R. E. (2018). Variational continual learning. In *International Conference on Learning Representations*
- Nilsson, G., Tamm, S., d'Onofrio, P., Thuné, H. Å., Schwarz, J., Lavebratt, C., et al. (2016). A multimodal brain imaging dataset on sleep deprivation in young and old humans
- Nooner, K. B., Colcombe, S., Tobe, R., Mennes, M., Benedict, M., Moreno, A., et al. (2012). The NKI-Rockland sample: A model for accelerating the pace of discovery science in psychiatry. *Frontiers in Neuroscience* 6, 152
- O'toole, A. J., Jiang, F., Abdi, H., and Haxby, J. V. (2005). Partially distributed representations of objects and faces in ventral temporal cortex. *Journal of cognitive neuroscience* 17, 580–590
- O'Connor, D., Potler, N. V., Kovacs, M., Xu, T., Ai, L., Pellman, J., et al. (2017). The healthy brain network serial scanning initiative: a resource for evaluating inter-individual differences and their reliabilities across scan conditions and sessions. *Gigascience* 6, 1–14
- Padmanabhan, A., Geier, C. F., Ordaz, S. J., Teslovich, T., and Luna, B. (2011). Developmental changes in brain function underlying the influence of reward processing on inhibitory control. *Developmental cognitive neuroscience* 1, 517–529
- Petersen, R. C., Aisen, P., Beckett, L., Donohue, M., Gamst, A., Harvey, D., et al. (2010). Alzheimer's disease neuroimaging initiative (adni): clinical characterization. *Neurology* 74, 201–209
- Poldrack, R. A., Barch, D. M., Mitchell, J., Wager, T., Wagner, A. D., Devlin, J. T., et al. (2013). Toward open sharing of task-based fmri data: the openfmri project. *Frontiers in neuroinformatics* 7, 12
- Power, J. D., Plitt, M., Kundu, P., Bandettini, P. A., and Martin, A. (2017). Temporal interpolation alters motion in fmri scans: Magnitudes and consequences for artifact detection. *PLoS one* 12, e0182939
- Repovs, G. and Barch, D. M. (2012). Working memory related brain network connectivity in individuals with schizophrenia and their siblings. *Frontiers in human neuroscience* 6, 137
- Robbins, H. and Monro, S. (1951). A stochastic approximation method. *The Annals of Mathematical Statistics* , 400–407
- Rohlfing, T. (2012). Image similarity and tissue overlaps as surrogates for image registration accuracy: widely used but unreliable. *IEEE transactions on medical imaging* 31, 153–163
- Romaniuk, L., Pope, M., Nicol, K., Steele, D., and Hall, J. (2016). Neural correlates of fears of abandonment and rejection in borderline personality disorder. *Wellcome Open Research* 1
- Ronneberger, O., Fischer, P., and Brox, T. (2015). U-net: Convolutional networks for biomedical image segmentation. In *International Conference on Medical Image Computing and Computer-Assisted Intervention* (Springer), 234–241
- Roy, A., Bernier, R. A., Wang, J., Benson, M., French Jr, J. J., Good, D. C., et al. (2017). The evolution of cost-efficiency in neural networks during recovery from traumatic brain injury. *PLoS One* 12, e0170541
- Roy, A. G., Conjeti, S., Navab, N., and Wachinger, C. (2018a). Bayesian quicknat: Model uncertainty in deep whole-brain segmentation for structure-wise quality control. *arXiv preprint arXiv:1811.09800*
- Roy, A. G., Conjeti, S., Navab, N., and Wachinger, C. (2018b). QuickNAT: Segmenting MRI neuroanatomy in 20 seconds. *arXiv preprint arXiv:1801.04161*

- Schonberg, T., Fox, C. R., Mumford, J. A., Congdon, E., Trepel, C., and Poldrack, R. A. (2012). Decreasing ventromedial prefrontal cortex activity during sequential risk-taking: an fmri investigation of the balloon analog risk task. *Frontiers in neuroscience* 6, 80
- Srivastava, N., Hinton, G., Krizhevsky, A., Sutskever, I., and Salakhutdinov, R. (2014). Dropout: a simple way to prevent neural networks from overfitting. *The Journal of Machine Learning Research* 15, 1929–1958
- Stephan-Otto, C., Siddi, S., Senior, C., Muñoz-Samons, D., Ochoa, S., Sánchez-Laforga, A. M., et al. (2017). Visual imagery and false memory for pictures: a functional magnetic resonance imaging study in healthy participants. *PloS one* 12, e0169551
- Tadel, F., Baillet, S., Mosher, J. C., Pantazis, D., and Leahy, R. M. (2011). Brainstorm: a user-friendly application for meg/eeeg analysis. *Computational intelligence and neuroscience* 2011, 8
- Titsias, M. K. and Lázaro-Gredilla, M. (2011). Spike and slab variational inference for multi-task and multiple kernel learning. In *Advances in neural information processing systems*. 2339–2347
- Tom, S. M., Fox, C. R., Trepel, C., and Poldrack, R. A. (2007). The neural basis of loss aversion in decision-making under risk. *Science* 315, 515–518
- Uncapher, M. R., Hutchinson, J. B., and Wagner, A. D. (2011). Dissociable effects of top-down and bottom-up attention during episodic encoding. *Journal of Neuroscience* 31, 12613–12628
- Van Essen, D. C., Smith, S. M., Barch, D. M., Behrens, T. E., Yacoub, E., Ugurbil, K., et al. (2013). The WU-Minn human connectome project: An overview. *NeuroImage* 80, 62–79
- Van Schuerbeek, P., Baeken, C., and De Mey, J. (2016). The heterogeneity in retrieved relations between the personality trait ‘harm avoidance’ and gray matter volumes due to variations in the vbm and roi labeling processing settings. *PloS one* 11, e0153865
- Velanova, K., Wheeler, M. E., and Luna, B. (2008). Maturation changes in anterior cingulate and frontoparietal recruitment support the development of error processing and inhibitory control. *Cerebral Cortex* 18, 2505–2522
- Verstynen, T. D. (2014). The organization and dynamics of corticostriatal pathways link the medial orbitofrontal cortex to future behavioral responses. *Journal of neurophysiology* 112, 2457–2469
- Vidorreta, M., Wang, Z., Chang, Y. V., Wolk, D. A., Fernández-Seara, M. A., and Detre, J. A. (2017). Whole-brain background-suppressed pcasl mri with 1d-accelerated 3d rare stack-of-spirals readout. *PloS one* 12, e0183762
- Vidorreta, M., Wang, Z., Rodríguez, I., Pastor, M. A., Detre, J. A., and Fernández-Seara, M. A. (2013). Comparison of 2d and 3d single-shot asl perfusion fmri sequences. *Neuroimage* 66, 662–671
- Vázquez, P. G., Whitfield-Gabrieli, S., Bauer, C. C., Barrios, and A, F. (2016). Brain functional connectivity of hypnosis without target suggestion. an intrinsic hypnosis rs-fmri study. (*under review*)
- Wager, T. D., Davidson, M. L., Hughes, B. L., Lindquist, M. A., and Ochsner, K. N. (2008). Prefrontal-subcortical pathways mediating successful emotion regulation. *Neuron* 59, 1037–1050
- Walz, J. M., Goldman, R. I., Carapezza, M., Muraskin, J., Brown, T. R., and Sajda, P. (2013). Simultaneous eeg-fmri reveals temporal evolution of coupling between supramodal cortical attention networks and the brainstem. *Journal of Neuroscience* 33, 19212–19222
- Wei, D., Zhuang, K., Chen, Q., Yang, W., Liu, W., Wang, K., et al. (2018). Structural and functional mri from a cross-sectional southwest university adult lifespan dataset (sald). *bioRxiv* , 177279
- Xue, G., Aron, A. R., and Poldrack, R. A. (2008). Common neural substrates for inhibition of spoken and manual responses. *Cerebral Cortex* 18, 1923–1932
- Yu, F. and Koltun, V. (2015). Multi-scale context aggregation by dilated convolutions. In *International Conference on Learning Representations*

Zuo, X.-N., Anderson, J. S., Bellec, P., Birn, R. M., Biswal, B. B., Blautzik, J., et al. (2014). An open science resource for establishing reliability and reproducibility in functional connectomics. *Scientific data* 1, 140049